



Synthesis of layered–layered $x\text{Li}_2\text{MnO}_3 \cdot (1-x)\text{LiMO}_2$ ($M = \text{Mn, Ni, Co}$) nanocomposite electrodes materials by mechanochemical process

Soo Kim^a, Chunjoong Kim^b, Jae-Kyo Noh^{a,c}, Seungho Yu^a, Su-Jin Kim^a, Wonyoung Chang^a, Won Chang Choi^a, Kyung Yoon Chung^{a,*}, Byung-Won Cho^{a,**}

^a Center for Energy Convergence, Korea Institute of Science and Technology, 39-1 Hawolgok-dong, Seongbuk-gu, Seoul 136-791, Republic of Korea

^b Environmental Energy Technologies Division, Lawrence Berkeley National Laboratory, Berkeley, CA 94720, USA

^c Department of Material Science and Engineering, Korea University, Seoul 136-701, Republic of Korea

HIGHLIGHTS

- Novel synthesis route for the Li_2MnO_3 -stabilized cathode which is time- and cost-efficient.
- Exact control of the amount of each component in $x\text{Li}_2\text{MnO}_3 \cdot (1-x)\text{LiMO}_2$ system.
- Confirmation of nanocomposite formation between the Li_2MnO_3 and LiMO_2 .

ARTICLE INFO

Article history:

Received 9 May 2012

Received in revised form

3 July 2012

Accepted 31 July 2012

Available online 9 August 2012

Keywords:

Lithium secondary battery

Cathodes

Mechanochemical process

Nanocomposite

ABSTRACT

A strategy of facile route to prepare the Li_2MnO_3 -stabilized LiMO_2 ($M = \text{Mn, Ni, Co}$) electrode materials, cathode materials for Lithium secondary batteries that can be operated at the high voltage greater than 4.5 V, is proposed using the method of mechanochemical process. Li_2MnO_3 was synthesized at 400 °C, followed by the mechanochemical process with LiMO_2 to form nanocomposite with the layered–layered structure. Structures and morphologies of $x\text{Li}_2\text{MnO}_3 \cdot (1-x)\text{LiMO}_2$ are investigated to confirm the layered–layered structural integration. Various mole ratios of our $x\text{Li}_2\text{MnO}_3 \cdot (1-x)\text{LiMO}_2$ electrode materials exhibit a large discharge capacity about 200 mAh g^{-1} at the room temperature. The cycle performances and the specific discharge capacities are improved by the secondary heat treatment for the $x\text{Li}_2\text{MnO}_3 \cdot (1-x)\text{LiMO}_2$ composite electrodes where $x \leq 0.5$. Our experimental results suggest the mechanochemical process is an easy and effective tool to form the nanocomposite of two components with controlled composition, especially, for the layered–layered integrated structure of $x\text{Li}_2\text{MnO}_3 \cdot (1-x)\text{LiMO}_2$ system.

© 2012 Elsevier B.V. All rights reserved.

1. Introduction

Lithium-ion batteries played a critical role in recent energy storage systems. A higher voltage candidate with a larger capacity is demanded to meet the requirements to satisfy the new energy storage systems [1–4]. Li_2MnO_3 has a theoretical capacity of 458 mAh g^{-1} operating above 4.5 V, in case all the lithium ions are utilized [5,6]. Li_2MnO_3 is believed to be electrochemically inactive because Mn has a valence of +4 and unlikely goes to a higher valence [7]. It was found that Li_2MnO_3 can be activated either chemically with the acid treatment or electrochemically to the removal of Li_2O [8], however, with a poor cycle performance due to

the structural changes [5]. Intensive research efforts are on-going to find the optimum electrodes system containing Li_2MnO_3 in two, or three components system, especially, $x\text{Li}_2\text{MnO}_3 \cdot (1-x)\text{LiMO}_2$ electrodes are highlighted to understand their structural, chemical, and electrochemical properties [8–12].

Electrochemical properties of $x\text{Li}_2\text{MnO}_3 \cdot (1-x)\text{LiMO}_2$ have been studied previously [5–13]. Synthesis of $x\text{Li}_2\text{MnO}_3 \cdot (1-x)\text{LiMO}_2$ is typically prepared from the co-precipitation process by adding excess lithium source to the metal hydroxide precursors, where Li reacts with Mn to form Li_2MnO_3 [8–12]. Li_2MnO_3 can be reformulated as $\text{Li}[\text{Li}_{1/3}\text{Mn}_{2/3}]\text{O}_2$, as well as $x\text{Li}_2\text{MnO}_3 \cdot (1-x)\text{LiMO}_2$ can be normalized to $\text{Li}_{1+(x/(2+x))}\text{M}'_{1+(x/(2+x))}\text{O}_2$ ($\text{M}' = \text{Mn} + \text{M}$, $0 < x < 1$), or $\text{Li}_{1+y}\text{M}'_{1-y}\text{O}_2$ for $y = (x/(2+x))$, (i.e. $\text{Li}_{1.05}(\text{Ni}_{0.33}\text{Co}_{0.33}\text{Mn}_{0.33})_{0.95}\text{O}_2$ is equivalent to $0.1\text{Li}_2\text{MnO}_3 \cdot 0.9\text{LiMn}_{0.26}\text{Ni}_{0.37}\text{Co}_{0.37}\text{O}_2$ [8]. It is very difficult, however, to confirm the exact stoichiometric yields in the composite because there are no quantitative analytical tools to exactly measure and monitor the synthesis process in co-precipitation, where the excess Li

* Corresponding author. Tel.: +82 2 958 5225; fax: +82 2 958 5229.

** Corresponding author. Tel.: +82 2 958 5222; fax: +82 2 958 5229.

E-mail addresses: kychung@kist.re.kr, kychung@gmail.com (K.Y. Chung), bwcho@kist.re.kr (B.-W. Cho).

reacts to Mn to form the stoichiometric amounts of Li_2MnO_3 during the heat treatment. Also, it is vague to quantify the amount of Li_2MnO_3 from the x-ray diffraction patterns of the composite due to the similarities in XRD patterns for Li_2MnO_3 and LiMO_2 , except the several weak peaks between 21 and $25^\circ 2\theta$, characterizing Li_2MnO_3 superlattice peaks. It requires more advanced analysis to predict the Mn valence, however, the valence stays as $+4$ for both in Li_2MnO_3 and LiMO_2 compounds [12], thus not able to verify the amount of Li_2MnO_3 . Finally, it is difficult to confirm and quantify the amount of Li_2MnO_3 via high-resolution transmission electronic microscopy, and also there is no guarantee that the Li_2MnO_3 component is uniformly dispersed in the two components system.

Recent study by West et al. found that the preparation of each component followed by the ball-milling-annealing process yields the same crystallographic and electrochemical features as those prepared by conventional methods for the layered-layered $0.5\text{Li}_2\text{MnO}_3 \cdot 0.5\text{LiNi}_{0.33}\text{Co}_{0.33}\text{Mn}_{0.33}\text{O}_2$ composite [13]. Until then, the researchers put numerous efforts to approve these two components are incorporated together in the interlayer spacing level [8]. We apparently know that the formation of Li_2MnO_3 plays a critical role in a layered-layered structure as the reservoir of the excess lithium sources as much as stabilizing the LiMO_2 component [6–16]. We demonstrated in our previous works that our mechanochemical process is an effective tool to form alloying among nanomaterials [17–20]. During our mechanochemical process, the zirconia bowl itself rotates, at the same time, the revolution occurs in the apparatus for an enhanced high-power-ball-milling. In the sidewall of the zirconia bowl, we built the constant space zone where the zirconia balls can more efficiently directed and rotate around the wall, in order to optimize the performance of the mechanochemical alloying as displayed in Fig. S1. In here, we demonstrate that Li_2MnO_3 and LiMO_2 can be incorporated together as the nanocomposite in a controlled mole ratio via mechanochemical process. We expect the two components electrode system to be closely and more precisely integrated with our facile process routes.

2. Experimental

2.1. Preparation

Li_2MnO_3 compounds are prepared from $\text{LiOH} \cdot \text{H}_2\text{O}$ (Aldrich) and $\text{MnCO}_3 \cdot x\text{H}_2\text{O}$ (Aldrich) with 2:1 stoichiometric ratio. The precursor were mixed by using a planetary mill in acetone (150 rpm, 1 h) followed by the heat treatment at 400°C in a box furnace for 32 h, adapted from Ref. [5]. Mechanochemical process was performed in a similar manner to our previous works using a planetary mill (FRITSCH Pulverisette 5) in wet-milling basis with acetone at 350 rpm for 3 h [17–20]. The ball-to-powder weight ratio was optimized at the ratio of 20:1. In order to yield the nanocomposites that each component can be closely incorporated, we also carried out the mechanochemical process (350 rpm, 3 h) with the commercially-available $\text{LiNi}_{0.5}\text{Co}_{0.2}\text{Mn}_{0.3}\text{O}_2$ (LNF Chemicals Corp., Korea, $\sim 10\ \mu\text{m}$) to obtain the nano-sized LiMO_2 (Fig. S2). The mechanochemical activation was performed with the various mole ratios of the two components of Li_2MnO_3 and LiMO_2 .

Li_2MnO_3 -stabilized LiMO_2 nanocomposites with the ratios of $0.3\text{Li}_2\text{MnO}_3 \cdot 0.7\text{LiMO}_2$, $0.5\text{Li}_2\text{MnO}_3 \cdot 0.5\text{LiMO}_2$, $0.7\text{Li}_2\text{MnO}_3 \cdot 0.3\text{LiMO}_2$, and $0.9\text{Li}_2\text{MnO}_3 \cdot 0.1\text{LiMO}_2$ were prepared with our mechanochemical process. Additional heat treatment was performed (1000°C , 10 h) to our samples to investigate whether there will be any major structural and electrochemical performance changes. All samples were each grinded in a mortar for about 2–3 min and we used the stainless steel test sieve (100 mm diameter \times 75 μm mesh) to remove any larger particles. Total of eight different composite samples as well as Li_2MnO_3 and $\text{LiNi}_{0.5}\text{Co}_{0.2}\text{Mn}_{0.3}\text{O}_2$ were

prepared for the structural analysis and the electrochemical performances in our studies.

2.2. Structure and morphology

Powder X-ray diffraction (XRD) measurements were performed using a Rigaku X-Ray Diffractometer using monochromatic $\text{Cu K}\alpha$ line at 40 kV and 100 mA for the measurements. The diffraction data were collected with a scan speed of $2^\circ\ \text{min}^{-1}$ over a 2θ range from 15° to 75° . For the XRD measurements to observe the effect of the temperature variations, the temperature was raised at a constant rate of $5^\circ\text{C}\ \text{min}^{-1}$, and the temperature was remained constant for 30 min when it reached at 400, 500, 600, 700, 800, 900, 1000 $^\circ\text{C}$. The morphology of $x\text{Li}_2\text{MnO}_3 \cdot (1-x)\text{LiMO}_2$ was characterized by scanning electron microscope (FE-SEM, NOVA NanoSEM200, FEI). For $0.5\text{Li}_2\text{MnO}_3 \cdot 0.5\text{LiMO}_2$ samples, high-resolution transmission electronic microscopy (HRTEM, Tecnai G2, FEI Company) was used to investigate the existence of two different crystal structures of Li_2MnO_3 and LiMO_2 . In addition, X-ray photoelectron spectroscopy (XPS, PHI 5000 VersaProbe, Ulvac-PHI) was employed to examine the surface bonding nature of the electrode materials.

2.3. Electrochemical measurements

Active materials were each mixed with Ketjen black (KB-500JD) and PVDF (SOLEF 5130, Solvay) in N-methyl-2-pyrrolidone (NMP) with a weight ratio of 93:3:4 to form a slurry. The slurry was mixed in a homogenizer for 1 h then coated onto an aluminum foil using a doctor blade and dried at oven for 2 h. The loading level of the electrodes were $2.5\text{--}3.5\ \text{mg}\ \text{cm}^{-2}$ with the initial thickness around $70\text{--}80\ \mu\text{m}$ including the aluminum foil (15 μm). The electrodes were rolled with a calendar press to a packing density of $2.2\text{--}2.8\ \text{g}\ \text{cm}^{-3}$. These electrodes are assembled in a dry room using Li metal as the counter and reference electrodes with a layer of separator in 2032 coin cell configuration (Hohsen Corp., Japan). Electrolyte with 1 M LiPF_6 in EC:DMC:DEC = 1:1:1 by volume was used. The cells were stored for 24 h to ensure complete impregnation of the electrodes and separators with the electrolyte. Galvanostatic charge-discharge cycling tests were carried out using a multichannel battery tester (Model 4000, Maccor Inc.) in a potential range of 2.0–4.8 V using a constant current/constant voltage (CC/CV) method for charging to 4.8 V and a CC method for discharging to 2.0 V with the typical test current of $10\ \text{mA}\ \text{g}^{-1}$ at the room temperature. Additionally, cyclic voltammetry (VSP, Bio-Logic) measurements were carried out to compare the differences between the $0.5\text{Li}_2\text{MnO}_3 \cdot 0.5\text{LiMO}_2$ and heat-treated $0.5\text{Li}_2\text{MnO}_3 \cdot 0.5\text{LiMO}_2$ electrodes materials.

3. Results and discussion

3.1. Structure and morphology

The crystal structure analysis of the powdered samples was performed with the X-ray diffraction measurements. Fig. 1 shows the resulting XRD profiles of Li_2MnO_3 (A), $\text{LiNi}_{0.5}\text{Co}_{0.2}\text{Mn}_{0.3}\text{O}_2$ (B), layered-layered nanocomposites of 0.3A-0.7B, 0.5A-0.5B, 0.7A-0.3B, and 0.9A-0.1B, and heat-treated nanocomposites (H) of 0.3A-0.7B H, 0.5A-0.5B H, 0.7A-0.3B H, and 0.9A-0.1B H. All of the diffraction patterns were indexed and their lattice parameters are calculated based on a hexagonal structure, which belongs to the spaces group $R\bar{3}m$, as similar to Park et al. [21]. The lattice parameters, c/a ratio, and the volume of our samples are shown in Table 1. The diffraction patterns of our prepared samples clearly overlay Li_2MnO_3 and LiMO_2 . Weak peaks between 21 and $25^\circ 2\theta$ are shown

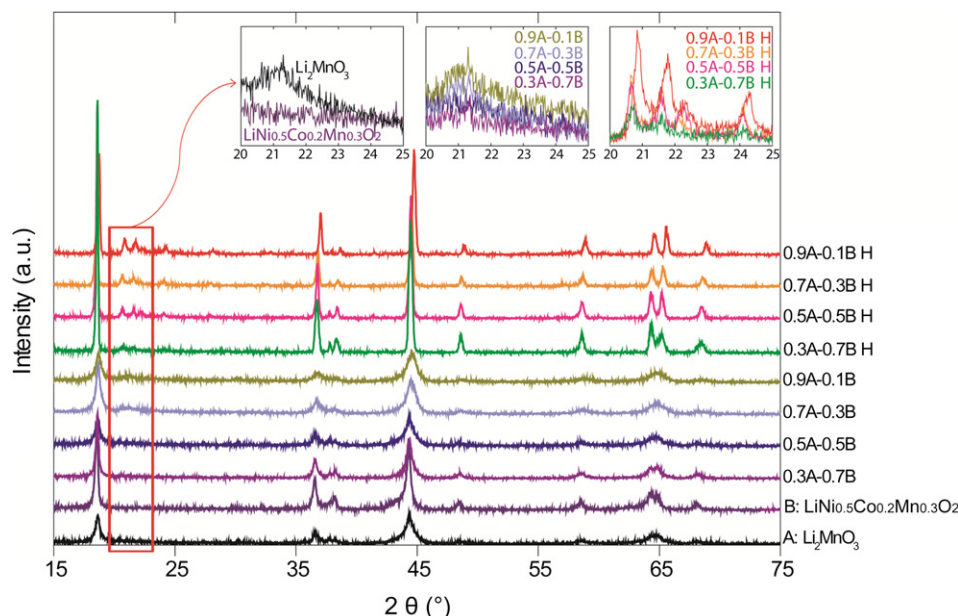


Fig. 1. XRD profiles of $x\text{Li}_2\text{MnO}_3 \cdot (1-x)\text{LiMO}_2$ ($0 \leq x \leq 1$).

at the top right corners, which indicate the cation ordering occurring in the transition metal layer of Li_2MnO_3 , consistent with those reported previously [5–13]. For $\text{LiNi}_{0.5}\text{Co}_{0.2}\text{Mn}_{0.3}\text{O}_2$, there are no peaks displayed between 21 and 25° 2θ . As more amounts of Li_2MnO_3 was inserted to the nanocomposite with our mechanochemical process, the intensities of weak peaks between 21 and 25° 2θ appear to increase. Furthermore, secondary heat treatment samples, 0.3A-0.7B H, 0.5A-0.5B H, and 0.7A-0.3B H have peaks at 20.6, 21.5, and 24.1° 2θ with higher intensities compared with the untreated nanocomposites. XRD peak shifts are observed for 0.9A-0.1B H, displaying peaks at 20.9, 21.8, and 24.3°. A double peak at 64.7° and 65.7° is also observed for the $\text{LiNi}_{0.5}\text{Co}_{0.2}\text{Mn}_{0.3}\text{O}_2$ and the secondary heat treatment samples. For our samples with the secondary heat treatment, we found the intensities of the peaks were remarkably increased, which we will discuss in the later section that the increase in the crystallinity could attribute to the cycle performance enhancement.

To monitor the phase transitions of our prepared nanocomposite, a high-temperature XRD technique was employed to examine the structural changes during the heat treatment. Fig. 2 shows the structural changes as the temperature is raised up to 1000 °C for the powdered sample of $0.5\text{Li}_2\text{MnO}_3 \cdot 0.5\text{LiNi}_{0.5}\text{Co}_{0.2}\text{Mn}_{0.3}\text{O}_2$ material. As the temperature increases, the overall intensities of the peaks increase. Weak peaks between 21 and 25°

2θ become apparent with increasing temperature, which again indicates the crystallinity improvement of the Li_2MnO_3 component, as well as the double peak around 65° 2θ is observed more apparently with the increasing temperature. Peaks at ~26, ~36, and ~43° 2θ indicate the Al_2O_3 peak from the aluminum oxide XRD holder.

Additionally, XPS study has been conducted to exactly identify the surface chemical states of the two component systems before and after the heat treatment. Fig. 3 shows XPS spectra of each element of Ni, Co, Mn, and O for $0.5\text{Li}_2\text{MnO}_3 \cdot 0.5\text{LiMO}_2$ and heat-treated $0.5\text{Li}_2\text{MnO}_3 \cdot 0.5\text{LiMO}_2$ electrode materials. For Ni, Co, and Mn, there is no obvious peak shift, however, overall peak intensities change after heat treatment. The $2p_{3/2}$ binding energies of Ni, Co, and Mn were ~854.3, 779.9, 642 eV corresponding to NiO , Co_2O_3 , and MnO_2 compounds, which represents our $x\text{Li}_2\text{MnO}_3 \cdot (1-x)\text{LiMO}_2$ samples have the chemical states Ni^{+2} , Co^{+3} , Mn^{+4} , which are comparable to those prepared with the conventional methods [6–12]. Interestingly, for O 1s, clear double peaks were detected at 528.5 eV from the lattice oxide ion and 531 eV from lithium carbonate. We believe that the Li_2CO_3 formation at the surface may be occurred during the mechanochemical process that the Li source may react with available CO_2 during the mixing [22–26]. However, the oxygen peak shows the intensity changes after the heat treatment. It is believed that Li_2CO_3 decomposed during the heat treatment, which explains the oxygen peak intensity ratio changes and the overall intensities changes from the XPS studies.

Fig. 4(a), (b), and (c) shows the SEM images of $0.5\text{Li}_2\text{MnO}_3 \cdot 0.5\text{LiMO}_2$ prepared by the mechanochemical process. The SEM images were prepared with the resolution of $\times 20,000$ for Fig. 4(a) and (b), and $\times 1000$ for Fig. 4(c). We observe that the primary particle sizes significantly increased with the heat treatment as shown in Fig. 4(a) and (b). We also observe the spherical secondary particle formations (~ μm scale) with the secondary heat treatments in Fig. 4(c), while the pristine $0.5\text{Li}_2\text{MnO}_3 \cdot 0.5\text{LiMO}_2$ exists as the nano-sized primary particles as displayed in Fig. 4(a). Fig. S3 also shows the SEM images 0.7A-0.3B H and 0.9A-0.1B H, which all display the formations of the spherical secondary particles. Again, all of our samples were treated with the mechanochemical process. With the heat treatment, it could yield more stable morphology from the mechanically-created disordered state

Table 1

Lattice parameters and c/a ratio of various $x\text{Li}_2\text{MnO}_3 \cdot (1-x)\text{LiMO}_2$; the structure was carefully refined to the space group $R\bar{3}m$.

Samples	<i>a</i>	<i>c</i>	<i>c/a</i>	Volume/ \AA^3
Li_2MnO_3 (A)	2.8503	14.1702	4.9715	99.69
$\text{LiNi}_{0.5}\text{Co}_{0.2}\text{Mn}_{0.3}\text{O}_2$ (B)	2.8761	14.2929	4.9695	102.39
0.3A-0.7B	2.8773	14.2775	4.9621	102.37
0.5A-0.5B	2.8775	14.2564	4.9545	102.22
0.7A-0.3B	2.8676	14.2762	4.9784	101.66
0.9A-0.1B	2.8591	14.2260	4.9758	100.70
0.3A-0.7B H ^a	2.8635	14.2715	4.9839	101.34
0.5A-0.5B H ^a	2.8599	14.2868	4.9955	101.19
0.7A-0.3B H ^a	2.8556	14.2626	5.0016	100.86
0.9A-0.1B H ^a	2.8465	14.2250	4.9974	99.81

^a H denotes samples with the secondary heat treatment (1000 °C, 10 h).

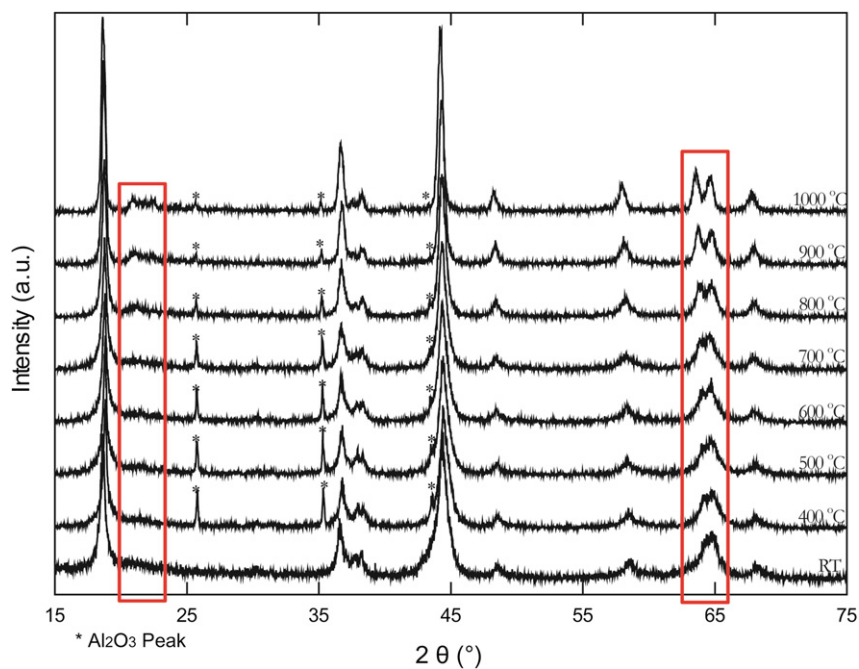


Fig. 2. Structural change of $0.5\text{Li}_2\text{MnO}_3 \cdot 0.5\text{LiMO}_2$ with temperature variations.

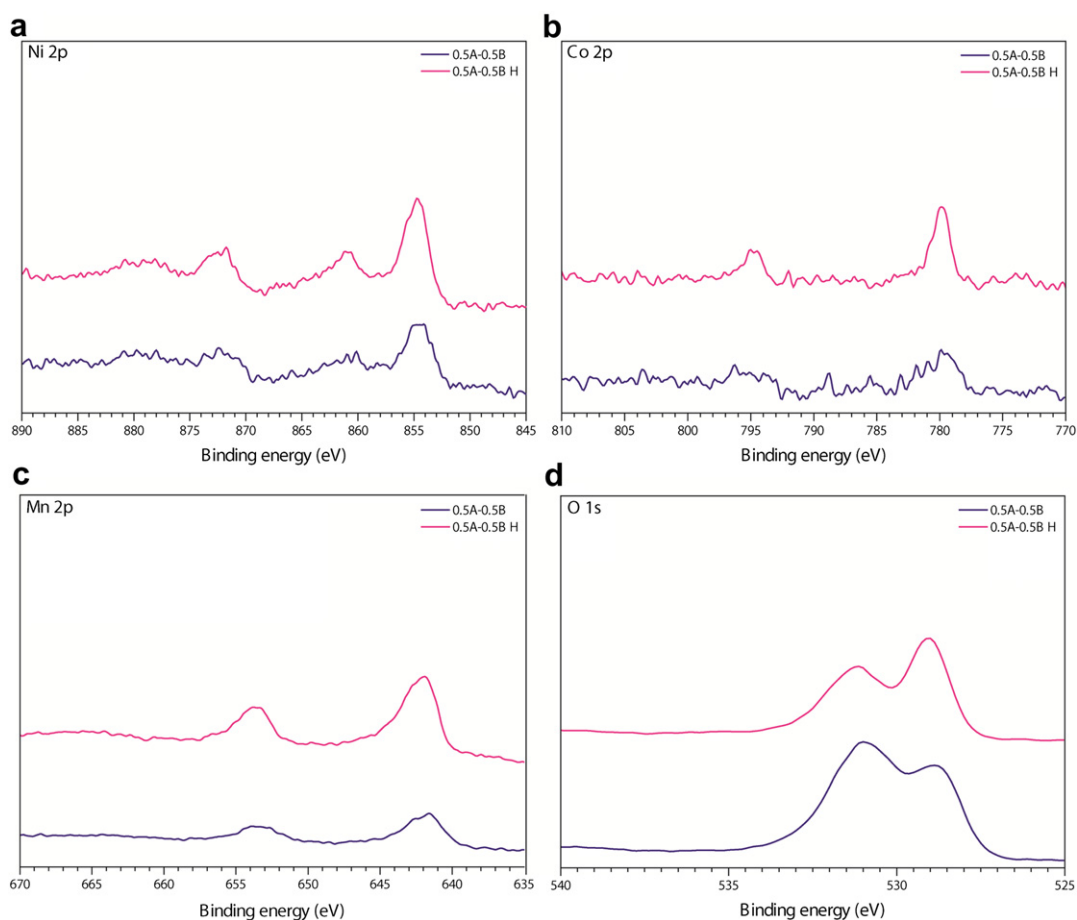


Fig. 3. XPS spectra of $0.5\text{Li}_2\text{MnO}_3 \cdot 0.5\text{LiMO}_2$ and heat-treated sample: (a) Ni 2p (b) Co 2p (c) Mn 2p (d) O 1s.

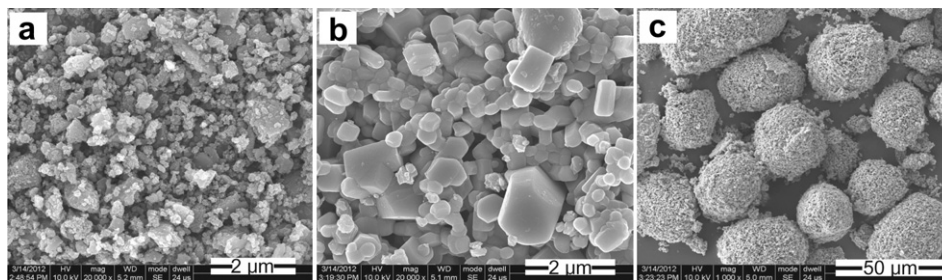


Fig. 4. SEM images of $x\text{Li}_2\text{MnO}_3 \cdot (1-x)\text{LiMO}_2$: (a) $0.5\text{Li}_2\text{MnO}_3 \cdot 0.5\text{LiMO}_2$ ($\times 20,000$) (b) $0.5\text{Li}_2\text{MnO}_3 \cdot 0.5\text{LiMO}_2$ H ($\times 20,000$) (c) $0.5\text{Li}_2\text{MnO}_3 \cdot 0.5\text{LiMO}_2$ H ($\times 1000$).

caused by the high-power-ball-milling; in this case, we believe that our nano-sized primary particles highly aggregated with the spherical-shaped secondary particles formations during the heat treatment. Won et al. reported the solid-state route to prepare the spherical yttrium aluminum garnet, which the ball-mill technique and the high-temperature treatment were performed [27]. McGuinness et al. and Chang et al. also carried out the mechanochemical alloying followed by the heat treatment to yield spherical-shaped $\text{Sm}_{1.15}\text{Co}_5$ and spherical-shaped mesocarbon microbeads (MCMB) secondary particles [28,29]. It is well known that the heat treatment process cause the particle growth and aggregations, however, these effects are escalated when the nanoparticles are prepared with the mechanochemical process and processed with the high-temperature heat treatment [27–29]. We report in the next section that the spherical secondary particle formations as well as the increase in the crystallinity greatly contribute on the cycle performance of the $0.5\text{Li}_2\text{MnO}_3 \cdot 0.5\text{LiMO}_2$.

To confirm that mechanochemical process yields the system of layered–layered structures, HRTEM is used to detect both Li_2MnO_3 and LiMO_2 in $0.5\text{Li}_2\text{MnO}_3 \cdot 0.5\text{LiMO}_2$ samples, the pristine and the heat-treated samples as displayed in Fig. 5(a) and (b). As illustrated in HRTEM images of $0.5\text{Li}_2\text{MnO}_3 \cdot 0.5\text{LiMO}_2$ composites, C2/m Li_2MnO_3 and $R\bar{3}m$ LiMO_2 components are respectively observed, consistent with those reported previously [6–12]. For the $0.5\text{Li}_2\text{MnO}_3 \cdot 0.5\text{LiMO}_2$ sample prepared immediately after the mechanochemical process, Li_2MnO_3 and LiMO_2 are each found in two adjacent primary particles that mechanochemically alloyed together, as shown in Fig. 5(a). We were able to segregate a small particle from the secondary spherical-shaped particle in the sample preparation for the secondary heat treatment sample. As displayed in Fig. 5(b), the integrated structures of Li_2MnO_3 and LiMO_2 are found in the single particle for the heat-treated sample. From the HRTEM images, we conclude that the use of the heat treatment may

ease the formation toward a closely intact nanocomposite for the layered–layered structure.

We further investigated $0.5\text{Li}_2\text{MnO}_3 \cdot 0.5\text{LiMO}_2$ samples with the energy-dispersive X-ray spectroscopy (EDS) to compare the element compositions as shown in Fig. 6(a), (b), (c), and (d). In all EDS analysis, element Cu is observed from the TEM grid. Please note that the EDS analysis does not provide exact amounts for each element, however, the relative comparisons can be made using the analysis results. The images on the upper corner indicate the HRTEM images for the point element analysis. We chose an arbitrary spot for the analysis, indicated by the red-circle. The analysis results of the pristine sample without the heat treatment are shown in Fig. 6(a), (b), and (c). From Fig. 6(a), the element composition ratios of Ni:Mn:Co = 5:3:2 can be approximated, where this region is most likely composed of $\text{LiNi}_{0.5}\text{Co}_{0.2}\text{Mn}_{0.3}\text{O}_2$. The chemical element with the most counts is Mn as shown in Fig. 6(c), and we are positive that that this region is mainly composed with Li_2MnO_3 . The pristine sample possesses each region of Li_2MnO_3 and LiMO_2 , we also identified the region that both Li_2MnO_3 and LiMO_2 co-exist as displayed in Fig. 6(b). We find that the element composition ratios of Ni:Mn:Co are approximately the average values from the Fig. 6(a) and (c). We analyzed the heat-treated $0.5\text{Li}_2\text{MnO}_3 \cdot 0.5\text{LiMO}_2$ in Fig. 6(d), and there are not much differences in the element compositions at various regions, which indicates the formation of the uniform nanocomposite throughout with the secondary heat treatment. The curve A (red-orange) shows the point element analysis of the outer particle, and the curve B (blue) indicates the inner particle composition in Fig. 6(d). Our prepared $0.5\text{Li}_2\text{MnO}_3 \cdot 0.5\text{LiMO}_2$ ($M = \text{Ni}_{0.5}\text{Co}_{0.2}\text{Mn}_{0.3}$) can be also notated as $\text{Li}_{1.2}(\text{Mn}_{0.65}\text{Ni}_{0.25}\text{Co}_{0.1})_{0.8}\text{O}_2$, and we find that the element counts from the y-axis agree very well with these compositions in Fig. 6(d). We strongly believe that the mechanochemical process effectively creates

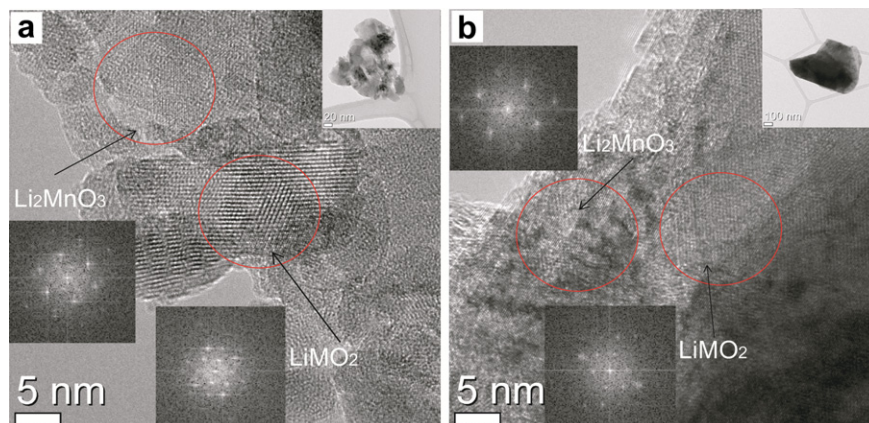


Fig. 5. HRTEM images: (a) $0.5\text{Li}_2\text{MnO}_3 \cdot 0.5\text{LiMO}_2$ (b) $0.5\text{Li}_2\text{MnO}_3 \cdot 0.5\text{LiMO}_2$ H.

nanocomposites with the adjacent regions where the two components alloy together as demonstrated in Fig. 6(b); and the heat treatment will aid the formation of the integrated structure as we demonstrated in Fig. 5(b) and Fig. 6(d).

3.2. Electrochemical measurements

Charge and discharge measurements on cells containing $x\text{Li}_2\text{MnO}_3 \cdot (1-x)\text{LiMO}_2$ as the active cathode material were carried out in the voltage range of 2.0–4.8 V. Fig. 7 shows the charge and discharge profile of the first cycle for the $x\text{Li}_2\text{MnO}_3 \cdot (1-x)\text{LiMO}_2$ prepared by the mechanochemical process as well as the pristine Li_2MnO_3 and LiMO_2 . With increasing amount of Li_2MnO_3 , the discharge capacities slightly increase, contributing from the high capacities of Li_2MnO_3 component. For the cell containing $0.3\text{Li}_2\text{MnO}_3 \cdot 0.7\text{LiMO}_2$, the discharge capacity of 173.4 mAh g^{-1} is obtained. The discharge capacity of 197.6 mAh g^{-1} is obtained for the $0.5\text{Li}_2\text{MnO}_3 \cdot 0.5\text{LiMO}_2$. The increase in the discharge capacities is observed, 199.3 and 205.7 mAh g^{-1} for the cells containing $0.7\text{Li}_2\text{MnO}_3 \cdot 0.3\text{LiMO}_2$ and $0.9\text{Li}_2\text{MnO}_3 \cdot 0.1\text{LiMO}_2$, respectively.

Fig. 8 shows the charge and discharge profile of the first cycle after the secondary heat treatment (1000°C , 10 h). The increase in the discharge capacities for $0.3\text{Li}_2\text{MnO}_3 \cdot 0.7\text{LiMO}_2$ and $0.5\text{Li}_2\text{MnO}_3 \cdot 0.5\text{LiMO}_2$ is observed, with the specific capacity of 184.9 and

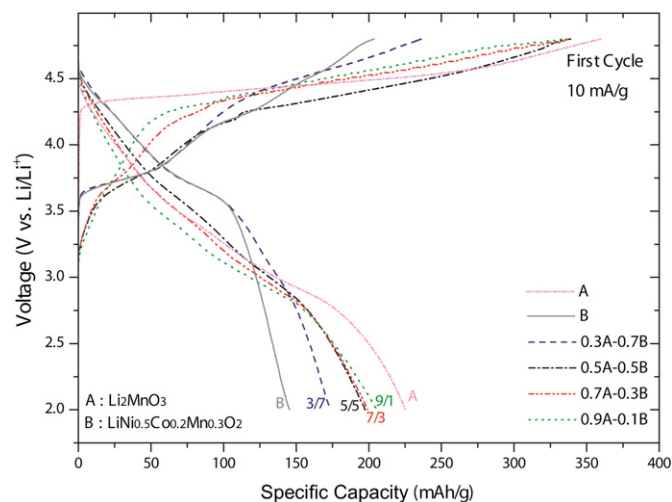


Fig. 7. First cycle charge-discharge of $x\text{Li}_2\text{MnO}_3 \cdot (1-x)\text{LiMO}_2$ ($0 \leq x \leq 1$).

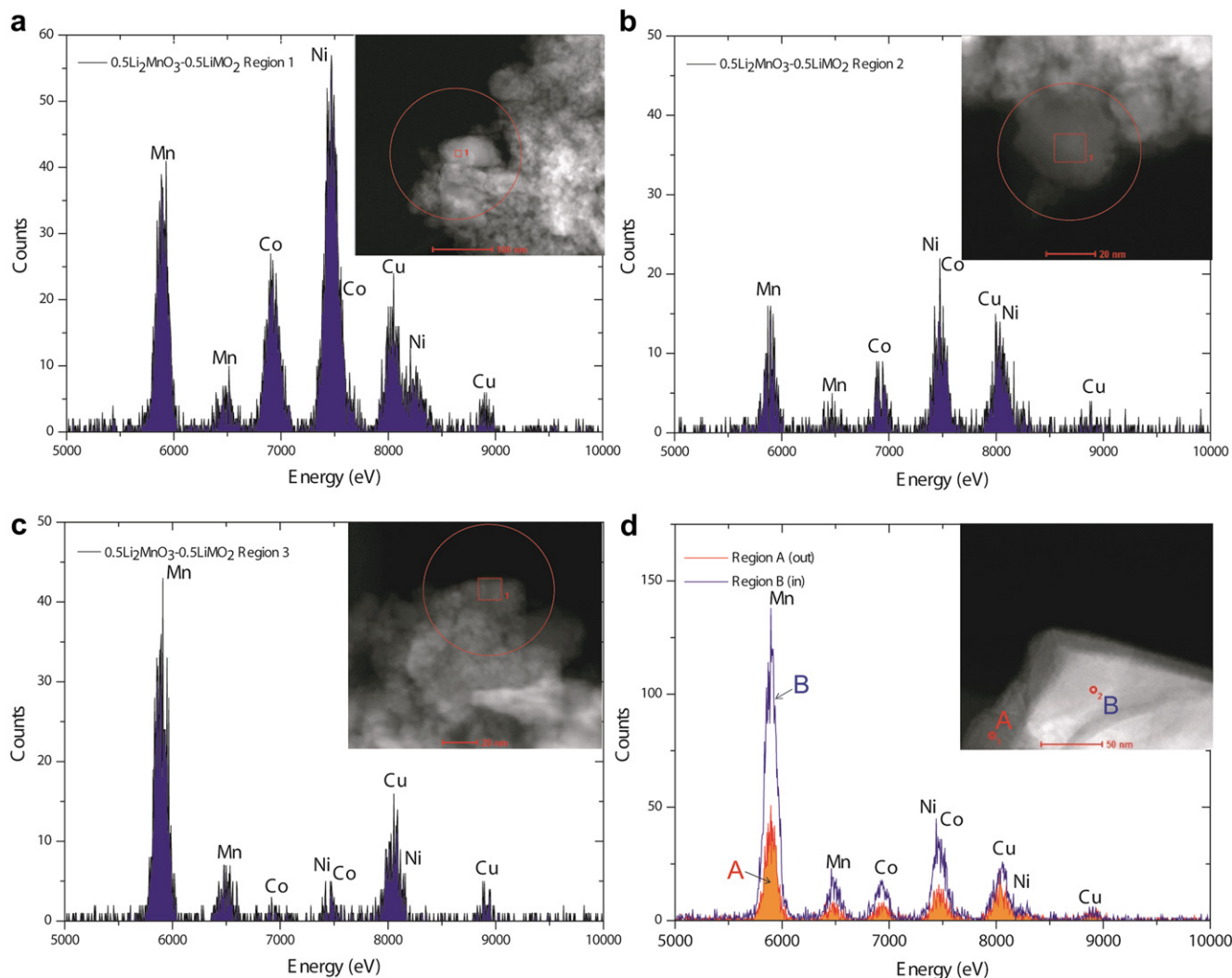


Fig. 6. EDS analysis of $0.5\text{Li}_2\text{MnO}_3 \cdot 0.5\text{LiMO}_2$: (a) $0.5\text{Li}_2\text{MnO}_3 \cdot 0.5\text{LiMO}_2$ (LiMO_2 -like region) (b) $0.5\text{Li}_2\text{MnO}_3 \cdot 0.5\text{LiMO}_2$ (mid-region) (c) $0.5\text{Li}_2\text{MnO}_3 \cdot 0.5\text{LiMO}_2$ (Li_2MnO_3 -like region) (d) $0.5\text{Li}_2\text{MnO}_3 \cdot 0.5\text{LiMO}_2$ H.

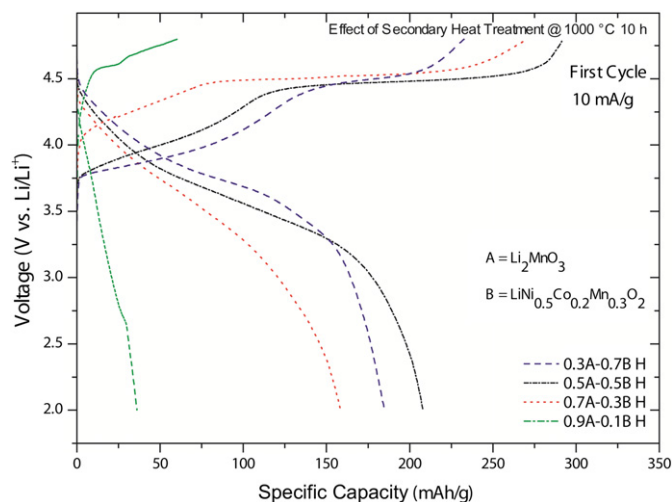


Fig. 8. First cycle charge-discharge of $x\text{Li}_2\text{MnO}_3 \cdot (1-x)\text{LiMO}_2$ H.

208.0 mAh g^{-1} , after the heat treatment. However, the discharge capacities for both $0.7\text{Li}_2\text{MnO}_3 \cdot 0.3\text{LiMO}_2$ and $0.9\text{Li}_2\text{MnO}_3 \cdot 0.1\text{LiMO}_2$ decreased after the heat treatment, with the specific capacities of 158.5 and 36.1 mAh g^{-1} . It was reported that the discharge capacities of Li_2MnO_3 significantly decrease with the increasing temperature, due to the more stable structure formation of Li_2MnO_3 at the higher temperature [5]. As more Li_2MnO_3 is incorporated in the composites of $0.7\text{Li}_2\text{MnO}_3 \cdot 0.3\text{LiMO}_2$ and $0.9\text{Li}_2\text{MnO}_3 \cdot 0.1\text{LiMO}_2$, the discharge capacities decrease significantly as the electrochemical properties of Li_2MnO_3 component is more dominantly displayed with the high temperature treatment.

Table 2 summarize the charge and discharge capacities of the first and second cycle for various $x\text{Li}_2\text{MnO}_3 \cdot (1-x)\text{LiMO}_2$ composites with a test current of 10 mA g^{-1} , and the charge and discharge capacities for Li_2MnO_3 and $\text{LiNi}_{0.5}\text{Co}_{0.2}\text{Mn}_{0.3}\text{O}_2$. From Table 2, we observe significant capacity losses between the first and the second cycle for $\text{LiNi}_{0.5}\text{Co}_{0.2}\text{Mn}_{0.3}\text{O}_2$, Li_2MnO_3 , and the $x\text{Li}_2\text{MnO}_3 \cdot (1-x)\text{LiMO}_2$ without the secondary heat treatment. However, we find that the secondary heat treatment samples have no loss of capacities between the first and the second cycle for the electrochemical test measurements with 2.0–4.8 V cutoff voltages.

Detailed reaction mechanism was studied by steady state cyclic voltammogram (CVs) in the composite electrodes comprising $0.5\text{Li}_2\text{MnO}_3 \cdot 0.5\text{LiMO}_2$ and the secondary heat treatment sample as the active mass with different charge cutoff potentials, with a scan rate of $100 \mu\text{V s}^{-1}$ (Fig. S4). The redox peak at 3.8/3.9 V corresponds to $\text{Ni}^{+2}/\text{Ni}^{+4}$ redox reaction in the Li–Ni–Co–Mn oxide lattice. The

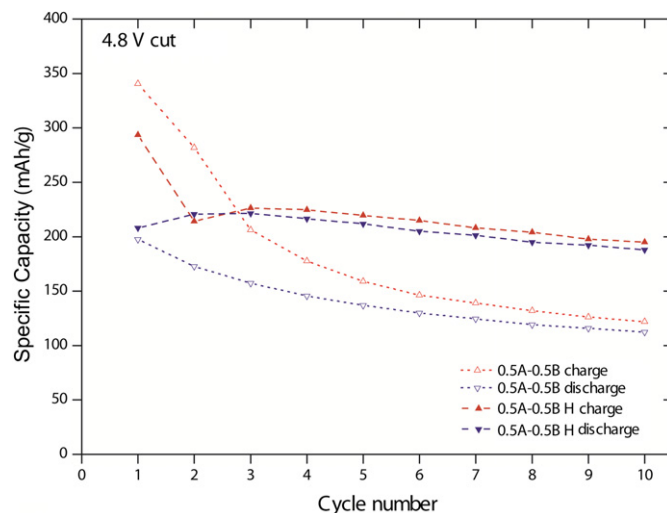


Fig. 9. Cycle characteristics of $0.5\text{Li}_2\text{MnO}_3 \cdot 0.5\text{LiMO}_2$ (10 Cycles, 10 mA g^{-1}).

high redox potential 4.3/4.4 V corresponds to $\text{Co}^{+3}/\text{Co}^{+4}$ redox reaction. Charging to high voltage above 4.5 V activates the Li_2MnO_3 component to be decomposed toward Li_2O and MnO_2 . Also, some irreversible capacities are observed after the first cycle CV after 4.5 V for $0.5\text{Li}_2\text{MnO}_3 \cdot 0.5\text{LiMO}_2$ without the secondary heat treatment. However, with the heat treatment, composite structure looks more integrated, leading to the intimate connection between Li_2MnO_3 and LiMO_2 , where Mn more effectively stabilizes the redox reaction. Thus, the loss of the capacity is mitigated and the peak at $\sim 3.7 \text{ V}$ become clear for the heat-treated $0.5\text{Li}_2\text{MnO}_3 \cdot 0.5\text{LiMO}_2$, which agrees very well with our galvanostatic charge-discharge cycling tests results.

The cycle characteristics for the coin cells containing $0.5\text{Li}_2\text{MnO}_3 \cdot 0.5\text{LiMO}_2$ and the heat-treated $0.5\text{Li}_2\text{MnO}_3 \cdot 0.5\text{LiMO}_2$ are shown in Fig. 9 for the ten consecutive cycles with 2.0–4.8 V cutoff voltages (10 mA g^{-1}). We observe significant capacities loss for $0.5\text{Li}_2\text{MnO}_3 \cdot 0.5\text{LiMO}_2$ without the secondary heat treatment. The cycle performance is significantly improved for the heat-treated $0.5\text{Li}_2\text{MnO}_3 \cdot 0.5\text{LiMO}_2$. We found earlier from the SEM images that after the secondary heat treatment at 1000°C 10 h, the size of the particles increased to form spherical shapes with the size range from $20 \mu\text{m}$ up to $40 \mu\text{m}$ for the larger particles. We believe that the high-temperature treatment ease the composite materials to become a better integrated nanostructure to enhance the cycle performance, also the formation of the uniform spherical-shaped particles with the heat treatment and the increase in the crystallinity significantly impact the improvement of the cycle performances.

4. Conclusion

Various mole ratios of $x\text{Li}_2\text{MnO}_3 \cdot (1-x)\text{LiMO}_2$ were prepared with the mechanochemical process and the electrochemical properties before and after the high-temperature heat treatment were tested. As proposed by West et al. [13], the variations of the stoichiometry were possible, and we initially found that the specific capacities increase with the increasing ratio of Li_2MnO_3 with the mechanical process without the heat treatment. Although the nanocomposite prepared with our process could yields a superior initial discharge capacity, the irreversible capacities, however, were very large for the samples without the secondary treatment. The secondary heat treatment at 1000°C improved the specific discharge capacities, when $x \leq 0.5$. When Li_2MnO_3 is the dominant component, the specific capacities are reduced due to the characteristics that the capacities of Li_2MnO_3

Table 2
Electrochemical properties of $x\text{Li}_2\text{MnO}_3 \cdot (1-x)\text{LiMO}_2$ (2.0–4.8 V cutoff).

Samples	Charge capacity (mAh g^{-1})	Discharge capacity (mAh g^{-1})	Charge capacity 2nd (mAh g^{-1})	Discharge capacity 2nd (mAh g^{-1})
Li_2MnO_3 (A) ^a	361.4	225.2	258.4	206.3
$\text{LiNi}_{0.5}\text{Co}_{0.2}\text{Mn}_{0.3}\text{O}_2$ (B)	215.4	145.4	176.3	136.8
0.3A-0.7B	248.0	173.4	161.0	142.6
0.5A-0.5B	340.7	197.6	281.7	172.6
0.7A-0.3B	338.9	199.3	244.1	185.5
0.9A-0.1B	334.6	205.7	248.1	189.3
0.3A-0.7B H ^b	244.7	184.9	193.4	190.71
0.5A-0.5B H ^b	293.6	208.0	214.3	220.7
0.7A-0.3B H ^b	272.4	158.5	183.8	168.1
0.9A-0.1B H ^b	62.2	36.1	48.6	43.4

^a Tested with different ratios of active material:binder:carbon = 80:10:10 (With Denka Black).

^b H denotes samples with the secondary heat treatment (1000°C , 10 h).

significantly decrease with the increasing temperature [5]. We also found the formation of the spherical-shaped secondary particles with the high-temperature treatment, which are typically observed in the time- and cost-intensive co-precipitation process [14–16]. With the increase in crystallinity and the formation of the spherical-shaped secondary particles, the cycle performances of the electrode materials were enhanced. We conclude that the optimized ratios of the two components enable the role of the stabilization for the Li_2MnO_3 , especially when $x \leq 0.5$. In this work, we also confirmed via HRTEM and EDS analysis that the high-temperature treatment yields the structural integration of the two components. We also suggest that two components do not necessarily need to be connected in an atomic level [8], as long as the Li_2MnO_3 and LiMO_2 exist as the nano-composite. Our process yields mechanically-alloyed layered–layered structural integrated nanomaterials, which display the similar structural and electrochemical properties from the conventional preparations.

Acknowledgments

This work was supported by the National Research Foundation of Korea Grant funded by the Korean Government (MEST) (NRF-2011-C1AAA001-0030538) and by the Global Research Laboratory Program through the National Research Foundation of Korea (NRF), which is funded by the Ministry of Education, Science and Technology (MEST) (grant number: 2011-00115). This work was also supported by the Assistant Secretary for Energy Efficiency and Renewable Energy, Office of Vehicle Technologies of the U.S. Department of Energy under Contract No. DE-AC02-05CH11231.

Appendix A. Supplementary data

Supplementary data related to this article can be found at <http://dx.doi.org/10.1016/j.jpowsour.2012.07.135>.

References

- [1] J.M. Tarascon, M. Armand, *Nature* 414 (2001) 359–367.
- [2] K.M. Shaju, P.G. Bruce, *Adv. Mater.* 18 (2006) 2330–2334.
- [3] M.M. Thackeray, P.J. Johnson, L.A. de Picciotto, P.G. Bruce, J.B. Goodenough, *Mater. Res. Bull.* 19 (1984) 179–187.
- [4] A.K. Padhi, K.S. Nanjundaswamy, J.B. Goodenough, *J. Electrochem. Soc.* 144 (1997) 1188–1194.
- [5] D.Y.W. Yu, K. Yanagida, Y. Kato, H. Nakamura, *J. Electrochem. Soc.* 156 (2009) A417–A424.
- [6] C.S. Johnson, S.D. Korte, J.T. Vaughey, M.M. Thackeray, T.E. Bofinger, Y. Shao-Horn, S.A. Hackney, *J. Power Sources* 81–82 (1999) 491–495.
- [7] M.H. Rossouw, A. Kock, L.A. Picciotto, M.M. Thackeray, *Mat. Res. Bull.* 25 (1990) 173–182.
- [8] M.M. Thackeray, S.H. Kang, C.S. Johnson, J.T. Vaughey, R. Benedek, S.A. Hackney, *J. Mater. Chem.* 17 (2007) 3112–3125.
- [9] S.H. Kang, C.S. Johnson, J.T. Vaughey, K. Amine, M.M. Thackeray, *J. Electrochem. Soc.* 153 (2006) A1186–A1192.
- [10] M.M. Thackeray, S.H. Kang, C.S. Johnson, J.T. Vaughey, S.A. Hackney, *Electrochem. Commun.* 8 (2006) 1531–1538.
- [11] C.S. Johnson, N. Li, C. Lefief, M.M. Thackeray, *Electrochem. Commun.* 9 (2007) 787–795.
- [12] S.H. Kang, P. Kempgens, S. Greenbaum, A.J. Kropf, K. Amine, M.M. Thackeray, *J. Mater. Chem.* 17 (2007) 2069–2077.
- [13] W.C. West, J. Soler, B.V. Ratnakumar, *J. Power Sources* 204 (2012) 200–204.
- [14] M.H. Lee, Y.J. Kang, S.T. Myung, Y.K. Sun, *Electrochim. Acta* 50 (2004) 939–948.
- [15] K.S. Lee, S.T. Myung, J.S. Moon, Y.K. Sun, *Electrochim. Acta* 53 (2008) 6033–6037.
- [16] Y.K. Sun, S.M. Myung, B.C. Park, J. Prakash, I. Belharouak, K. Amine, *Nat. Mater.* 8 (2009) 320–324.
- [17] H.C. Shin, S.B. Park, H. Jang, K.Y. Chung, W.I. Cho, C.S. Kim, B.W. Cho, *Electrochim. Acta* 53 (2008) 7946–7951.
- [18] Y.U. Kim, B.W. Cho, H.J. Sohn, *J. Electrochem. Soc.* 152 (2005) A1475–A1478.
- [19] S.G. Woo, J.H. Jung, H. Kim, M.G. Kim, C.K. Lee, H.J. Sohn, B.W. Cho, *J. Electrochem. Soc.* 153 (2006) A1979–A1983.
- [20] S.H. Oh, S.H. Jeon, W.I. Cho, C.S. Kim, B.W. Cho, *J. Alloys Compd.* 452 (2008) 389–396.
- [21] M.S. Park, J.W. Lee, W.C. Choi, D. Im, S.G. Doo, K.S. Park, *J. Mater. Chem.* 20 (2010) 7208–7213.
- [22] S. Verdier, L. El Ouatani, R. Dedryvere, F. Bonhomme, P. Biensan, D. Gonbeau, *J. Electrochem. Soc.* 154 (2007) A1088–A1099.
- [23] L. Daheron, R. Dedryvere, H. Martinez, D. Flahaut, M. Menetrier, C. Delmas, D. Gonbeau, *Chem. Mater.* 21 (2009) 5607–5616.
- [24] A.T. Appapillai, A.N. Mansour, J. Cho, Y. Shao-Horn, *Chem. Mater.* 19 (2007) 5748–5757.
- [25] G. Ceder, Y.M. Chiang, D.R. Sadoway, M.K. Aydinol, Y.I. Jang, B. Huang, *Nature* 392 (1998) 694–696.
- [26] J.P. Allain, D.L. Rokusek, S.S. Harilal, M. Nieto-Perez, C.H. Skinner, H.W. Kugel, B. Heim, R. Kaita, R. Majeski, *J. Nucl. Mater.* 390–391 (2009) 942–946.
- [27] C.W. Won, H.H. Nersisyan, H.I. Won, J.H. Lee, K.H. Lee, *J. Alloys Compd.* 509 (2011) 2621–2626.
- [28] P.J. McGuinness, S. Kobe, *J. Alloys Compd.* 281 (1998) 23–26.
- [29] Y.C. Chang, H.J. Sohn, C.H. Ku, Y.G. Wang, Y. Korai, I. Mochida, *Carbon* 37 (1999) 1285–1297.